Monoclinic symmetry of the hcp-type ordered areas in bulk cobalt

Paweł Kozłowski [1] Piotr Fabrykiewicz [1,2,3] Izabela Sosnowska [1] François Fauth [4] Anatoliy Senyshyn [5]
Emmanuelle Suard [6] Dariusz Oleszak [7] and Radosław Przenioslo [1,*]

[1]*Faculty of Physics, University of Warsaw, Pasteura 5, PL-02-093 Warsaw, Poland*
[2]*Institute of Crystallography, RWTH Aachen University, Jägerstraße 17-19, D-52066 Aachen, Germany*
[3]*Jülich Centre for Neutron Science at Heinz Maier-Leibnitz Zentrum, Forschungszentrum Jülich GmbH, Lichtenbergstraße 1,
D-85747 Garching, Germany*
[4]*CELLS-ALBA, Carrer de la Llum 2-26, ES-08290 Cerdanyola del Vallés, Barcelona, Spain*
[5]*Heinz Maier-Leibnitz Zentrum, Technical University of Munich, Lichtenbergstraße 1, D-85747 Garching, Germany*
[6]*Institut Laue-Langevin, 71 Av. des Martyrs, F-38000 Grenoble, France*
[7]*Faculty of Materials Science and Engineering, Warsaw University of Technology, Wołoska 141, PL-02-507 Warsaw, Poland*

The gradual ferromagnetic spin reorientation in hexagonal close packed cobalt (hcp-Co) phase between $230\,^\circ$C and $330\,^\circ$C reported for a Co single crystal [Bertaut *et al.*, Solid State Commun. **1**, 81 (1963)] suggests that this phase could not have a hexagonal symmetry. This hypothesis is verified positively by synchrotron radiation diffraction and neutron diffraction on polycrystalline powder cobalt. The analysis of diffraction data has been done by using a specific set of Bragg peaks, which are not sensitive to the stacking faults present in abundance in hcp-Co. The crystal structure of the hcp-type ordered areas of cobalt is described by the monoclinic symmetry with the magnetic space group $C2'/m'$. In this monoclinic crystal structure the former hexagonal [001] axis is no longer perpendicular to the hexagonal layers. The hexagonal [001] and [010] axes make an angle equal $\alpha \approx 90.10(1)\,^\circ$, while the angle between in-plane [100] and [010] axes equals $\gamma \approx 120.11(1)\,^\circ$. The monoclinic symmetry provides an approximate description of the crystal structure of the stacking faulted hcp-Co areas coexisting with fcc-Co areas.

I. INTRODUCTION

Cobalt is an extensively studied material with a layered-type structure, which can crystallize in two different orderings: the hexagonal-close-packed (hcp-Co) and the face centered-cubic (fcc-Co) [1]. The microstructure of the hcp and fcc phases of cobalt and similar layered materials was studied in the past decades by x-ray diffraction [2–6], neutron diffraction [7–9], and electron microscopy [10–13]. Electron microscopy studies show the presence of partial dislocations, which sometimes delimit domains of hcp-Co embedded in the fcc-Co matrix or vice versa, domains of fcc-Co embedded in a hcp-Co matrix [14,15]. The hcp-Co phase is associated with numerous stacking faults while the fcc-Co phase has considerably less stacking faults, as shown, e.g., in [2–9,16]. Two domains of hcp-Co stacked one above the other with a stacking fault in between are usually delimited by a small interface region of a few fcc-Co layers as shown, e.g., in [2,11,12]. The average hcp domain consists of 20 to 40 hexagonal layers before the next stacking fault occurs [6,8]. The crystal structure of fcc-Co has to be considered while analyzing the crystal structure of hcp-Co phase, because they are often clustered together in the same grains of cobalt.

The ferromagnetic spin reorientation process motivates the revisit of the symmetry and the crystal structure of

hcp-Co. Single crystal magnetization [17], single crystal neutron diffraction [18,19], and elastic properties measurements [20,21] show that between $230\,^\circ$C and $330\,^\circ$C the ferromagnetically aligned Co magnetic moments in hcp-Co single crystals gradually rotate from a direction parallel to [001] towards a direction perpendicular to [001]. Above $330\,^\circ$C the magnetic moments remain perpendicular to [001] up to about $400\,^\circ$C when the hcp-Co transforms to the fcc-Co [22]. In this paper the crystallographic planes and directions refer to the hexagonal system; when other systems are used it is given explicitly.

The crystal structure of the hcp-Co areas is assigned to the hexagonal space group $P6_3/mmc$ (no. 194). The ferromagnetic mode 00F with magnetic moments parallel to the hexagonal [001] axis (below $230\,^\circ$C) is compatible with the hexagonal symmetry as discussed in [23]. The magnetic space group $P6_3/mm'c'$ [24,25] is compatible with the mode 00F [23]. Ferromagnetic orderings with moments perpendicular to [001] are not compatible with any magnetic space group derived from $P6_3/mmc$ [24]. The gradual magnetic moment reorientation requires a ferromagnetic ordering of mode F0F, which is compatible with monoclinic symmetry [23]. The ferromagnetic ordering observed in hcp-Co above $230\,^\circ$C can be described by a monoclinic subgroup of $P6_3/mm'c'$. The hypothesis about the monoclinic symmetry drawn from observations of the magnetic properties of hcp-Co single crystals are studied in this paper with polycrystalline powder samples of cobalt. We use synchrotron radiation (SR) powder diffraction and neutron powder diffraction with one Co

sample, which is almost pure hcp-Co and another Co sample with about fcc:hcp molar ratio circa 18%:82%.

II. MATERIALS AND METHODS

In this study two commercial powder Co samples were used: the first labeled as HCP-Co (provided by Acros, Lot A0414657) is almost hcp-pure and the second, labeled as MIX-Co (provided by Alfa-Aesar, Lot 23997) is a mixture of phases with the molar ratio fcc:hcp = 18%:82%. The HCP-Co sample was divided in parts for use in neutron diffraction and synchrotron radiation (SR) diffraction measurements. Please note that we use the symbol with capital letters HCP-Co for the sample label and the symbol with lowercase letters hcp-Co for the hexagonal-close-packed phase of cobalt in general.

The first part of the HCP-Co sample was used for neutron powder diffraction measurements at RT using the instrument D2B at the Institut Laue-Langevin in Grenoble, France. The measurements were done at RT with long counting times to obtain high statistical accuracy. The sample was placed in an 8-mm-diameter vanadium container, the neutron wavelength was 1.5946 Å and the instrument was set in high intensity mode, i.e., using α_1 and α_2 fully open and $\alpha_3 = 5'$. The angular range was $10° < 2\theta < 162.5°$ corresponding to 0.11 Å^{-1} $< Q < 1.24$ Å^{-1}, where the scattering vector is defined as $Q = 2\sin(\theta)/\lambda$.

The second part of the HCP-Co sample was used for neutron powder diffraction measurements at the instrument SPODI [26] at the Heinz Maier-Leibnitz Zentrum in Garching, Germany. Measurements were performed with the HCP-Co sample placed in an 8-mm-diameter vanadium container at several temperature values between RT and $380°C$. The neutron wavelength was 1.5468 Å, and the instrument was in high intensity mode collimation, i.e., using α_1 and α_2 fully open and $\alpha_3 = 10'$. The angular range was $10° < 2\theta < 157°$ corresponding to 0.11 Å^{-1} $< Q < 1.26$ Å^{-1}. The temperature control was obtained using an ILL-type furnace.

SR diffraction measurements were done at the powder diffraction beamline BL04-MSPD [27] of the ALBA synchrotron in Cerdanyola del Valles, Spain. The powder HCP-Co and MIX-Co samples were sealed in 0.5-mm diameter borosilicate capillaries and transmission geometry was used. The operating wavelength was refined using a NIST standard silicon sample, NIST SI640D. Powder diffraction patterns were collected using the one-dimensional silicon based position-sensitive detector MYTHEN [28]. This setup allows fast data acquisition with better statistical accuracy as compared with the multi-analyser detector (MAD) setup [29] at the expense of angular resolution [30]. The instrumental resolution was estimated by measuring the SR powder diffraction pattern of $Na_2Ca_3Al_2F_{14}$ (NAC) reference standard [31].

The first session of measurements at MSPD beamline was done using a wavelength of $\lambda = 0.41301(4)$ Å at the angular range $2.4° < 2\theta < 72°$ (corresponding to 0.10 Å^{-1} $< Q < 2.84$ Å^{-1}) with the HCP-Co and MIX-Co at RT. This wavelength gives access to a large Q range and gives an optimal sample absorption.

The second session of measurements at MSPD beamline was done using a wavelength of $\lambda = 0.41357(6)$ Å at the angular range $2.4° < 2\theta < 82°$ (corresponding to 0.1 Å^{-1} $<$
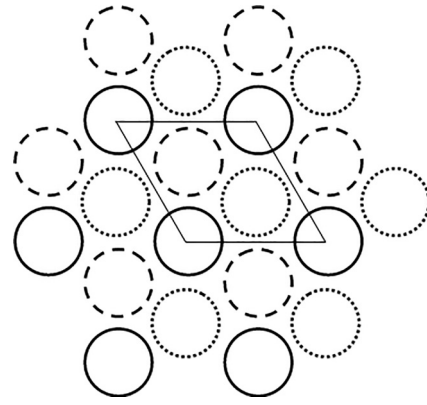

FIG. 1. In-plane atomic positions in the hexagonal A (solid line), B (dashed line), and C (dotted line) layers (adapted from [2]). The hexagonal unit cell is depicted with solid lines.

$Q < 3.17$ Å^{-1}). The MIX-Co sample was measured at temperatures 25, 100, 150, 200, and $250°C$. Temperature control was obtained by using a cryostream 700+ series model from Oxford Cryosytems flowing thermalized N_2 gas on the sample *in situ*.

III. RESULTS

A. Stacking of atomic layers in hcp-Co and fcc-Co areas, simplified model vs more realistic model

The hcp and fcc structures of cobalt are described as two different stacking arrangements of the atomic hexagonal layers drawn in Fig. 1: hcp is equivalent to an *ABABAB*...type stacking while fcc to an *ABCABC*...type stacking [2,3]. The in-plane atomic coordinates in hexagonal setting are A(0, 0), B($\frac{1}{3}$, $\frac{2}{3}$), and C($\frac{2}{3}$, $\frac{1}{3}$).

In the simplified model the cobalt crystallites can be described with set of well arranged layers, which fulfill the assumptions:

(i - simplified). The hexagonal layers have very few defects, i.e., the arrangement shown in Fig. 1 extends over large in-plane distances and there are small in-pane microstrains.

(ii - simplified). The hcp-type ordering can exist for less than 20–40 layers [2,6] and then a change of the layers' ordering (i.e., the stacking fault) must occur. The fcc-type ordering can be observed, e.g., for a few hundreds of layers. In both hcp and fcc areas the layers are well ordered at long in-plane distances.

(iii - simplified). The inter-layer d-spacing has the same value for any stacking sequence, i.e., the same for hcp-type, fcc-type order as well as in the vicinity of stacking faults.

This simplified model is often used by researchers for analyzing and simulating hcp-Co diffraction patterns, e.g., Frey *et al.* [8] and Sławiński *et al.* [16].

In a more realistic model of the crystal structure of cobalt it can be assumed that the previous simplified assumptions should be changed as follows:

(i - realistic). The hexagonal layers have numerous in-plane defects as shown by electron microscopy studies, e.g., [10–13]. It means that the arrangement shown in Fig. 1 extends over distances much smaller than in the simplified

model. There may be also considerable in-plane microstrains, which are larger than in the simplified model.

(ii - realistic). The stacking faults in the hcp-type arrangement are expected as in the simplified model, however please note the larger number of in-plane defects.

(iii - realistic). The inter-layer d-spacing for fcc-type order is larger by about 0.5% than for hcp-type order, so one can expect some microstrain along the [001] axis that is larger than in the simplified model.

B. Bragg peaks insensitive to stacking faults

In this simplified model of the crystal structure of cobalt one can expect two types of Bragg peaks: sensitive to stacking faults and not-sensitive to stacking faults. For the AB layers' sequence the Co atoms are located at $A(0, 0, \frac{1}{4})$ and $B(\frac{1}{3}, \frac{2}{3}, \frac{3}{4})$ and their contribution to the structure factor is proportional to $[1 + \exp(i\phi)]$ where

$$\phi = 2\pi \left\{ \frac{h}{3} + \frac{2k}{3} + \frac{l}{2} \right\} = 2\pi \left\{ \frac{h-k}{3} + k \right\} + \pi l. \quad (1)$$

For the AC layers' sequence we have $A(0, 0, \frac{1}{4})$ and $C(\frac{2}{3}, \frac{1}{3}, \frac{3}{4})$, so we obtain

$$\phi = 2\pi \left\{ \frac{2h}{3} + \frac{k}{3} + \frac{l}{2} \right\} = 2\pi \left\{ -\frac{h-k}{3} + h \right\} + \pi l. \quad (2)$$

For the BC layers' sequence we have $B(\frac{1}{3}, \frac{2}{3}, \frac{1}{4})$ and $C(\frac{2}{3}, \frac{1}{3}, \frac{3}{4})$, so we obtain

$$\phi = 2\pi \left\{ \frac{h-k}{3} \right\} + \pi l. \quad (3)$$

In all three cases the values of ϕ calculated in Eqs. (1)–(3) are multiples of 2π if

$$h - k = 3n_1, \quad (4a)$$

$$l = 2n_2, \quad (4b)$$

where n_1 and n_2 are both integers. With these conditions fulfilled for all possible sequences (excluding the same layers as nearest neighbors) every layer contributes to the structure factor with the same value, $e^{2\pi iN} = 1$ (with N integer). The Bragg peaks with indices that fulfill Eqs. (4a) and (4b) will be named as stacking-faults-insensitive, or shortly as "insensitive" peaks—because their structure factor is not affected by the stacking faults, as mentioned, e.g., by Edwards and Lipson [2]. The Bragg peaks, which do not fulfill Eqs. (4a) and (4b) are broadened and/or asymmetric due to stacking faults as explained in [2]. In this study we will use the following insensitive peaks of the hcp-Co phase model (sorted with decreasing d-spacing values): (002), (110), (112), (004), (114), (302), (006), (220).

C. Some limitations of the stacking-faults-insensitive peaks approach

The conditions given in Eqs. (1)–(4b) are too simplified for real cobalt samples. The coexistence of intertwined hcp-type and fcc-type domains with limited in-plane size may lead to an increase of anisotropic microstrains and to the broadening of the peaks labeled as "insensitive".
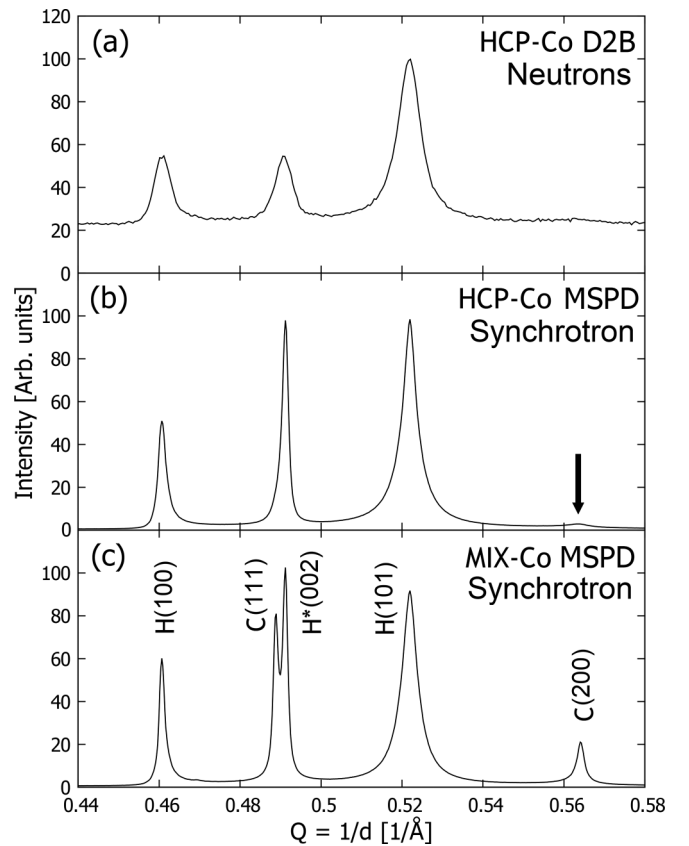

FIG. 2. Selected parts of neutron diffraction pattern of HCP-Co (a) and SR diffraction patterns of HCP-Co (b) and MIX-Co (c) samples at RT. The peaks due to hcp and fcc phase models are marked with "H" and "C" symbols, respectively. The stacking faults insensitive peak (002) is marked with (*). The very weak C(200) peak is shown with an arrow in panel (b). The scattering vector $Q = 2 \sin \theta / \lambda$, where 2θ is the scattering angle.

Another warning is related to the use of the terms hcp-Co phase and fcc-Co phase. In polycrystalline cobalt samples the stacked layers arranged in hcp-type and fcc-type order coexist in the same polycrystalline grains and the layers of fcc-type can increase the microstrain of the neighboring hcp-type layers (or vice versa), see e.g., [9]. Therefore the term phase is not completely appropriate. The powder diffraction measurements provide an oversimplified approximate model obtained by averaging over many intertwined areas, which contribute to Bragg peaks usually attributed to the hcp and fcc phases.

D. Comparison of neutron and synchrotron radiation diffraction patterns of the cobalt samples

Representative parts of the neutron and SR powder diffraction patterns of the HCP-Co and MIX-Co samples are shown in Fig. 2. The scattering vector Q is used as a common scale for easier visualization. The intensity is given in arbitrary units in which the highest peak has its maximum value 100. The diffraction patterns of the HCP-Co sample in Figs. 2(a) and 2(b) show one symmetric and narrow "insensitive" $H(002)$ peak and two peaks: $H(100)$ and $H(101)$ affected by stacking faults, i.e., $H(100)$ is asymmetric with a broad right side while

$H(101)$ is symmetric and broad. There is also one narrow and symmetric peak of the fcc-Co phase $C(200)$. The HCP-Co sample has the fcc:hcp molar ratio 2.5%:97.5% and only few separated weak fcc peaks can be observed, see e.g., the $C(200)$ near $Q = 0.565$ Å^{-1} marked with the arrow in Fig. 2(b). The sample HCP-Co can be considered as a collection of many stacking faulted hcp-Co domains separated by a small amount of fcc-Co domains.

The relatively high and almost flat background in the neutron diffraction pattern of HCP-Co [Fig. 2(a)] is due to the incoherent neutron scattering of the cobalt sample and the vanadium container [32]. The difference of peak-to-background ratios between neutron and SR diffraction patterns is due to the unfavourable ratio of the coherent and incoherent scattering lengths of cobalt: b(coh) = 2.49 fm and b(inc) = –6.2 fm [32]. The hcp-Co areas at RT have a ferromagnetic ordering with magnetic moments directed along [001], so the $H(002)$ Bragg peak has no magnetic neutron scattering contribution while both $H(100)$ and $H(101)$ have some.

The SR diffraction pattern of MIX-Co samples shows the molar ratio fcc:hcp about 18%:82%, see Fig. 2(c). Please note that the cubic $C(111)$ and hexagonal $H(002)$ peaks are separated because the average ABCABC and ABABAB interlayer distances for fcc-Co and hcp-Co differ by about 0.5%, see e.g., [33–35].

E. Analysis of shapes of stacking-faults' sensitive Bragg peaks

The well-established methodology of stacking faults models, see e.g., the book by Warren [36], was applied to the SR diffraction patterns of MIX-Co and HCP-Co samples. In this model two types of stacking faults are assumed: deformation faults with probability α_{ST} and growth faults with probability β_{ST}. The deformation faults add two local fcc stacking sequences, e.g., ...ABABCACACA..., where the local fcc sequences are (ABC) and (BCA). The growth faults add only one local fcc sequence, e.g., ...ABABCBCBC.., i.e., (ABC) is the only local fcc sequence. These two stacking fault types bring different contributions to the x-ray diffraction pattern [36].

The calculations have been done with the programme FAULTS [37] assuming the hexagonal and monoclinic symmetry of the hcp-type areas. The parameters of the monoclinic symmetry model are given in Sec. III G. We found a good agreement for the sensitive peaks with both models and the same probabilities $\alpha_{ST} = 0.0067$ and $\beta_{ST} = 0.03$, i.e., similar values to those found for powder cobalt samples in [6]. These probabilities correspond to an average column length of the hcp-type area $1/(\alpha_{ST} + \beta_{ST}) \approx 27$ layers (thickness 55 Å). The model shows satisfactory agreement for the stacking faults sensitive peaks, e.g., $H(202)$, $H(104)$, $H(203)$, see Fig. 3. Both HCP-Co and MIX-Co samples with different fcc contents (2.5% and 18%) and different microstrains, however, show similar shapes of the stacking faults sensitive peaks, see Fig. 3. The same model of stacking faults, both in hexagonal and monoclinic symmetry works well for both samples.

The main difference between the two patterns is due to the Bragg peaks of the fcc-Co phases, see e.g., $C(222)$, $C(400)$ present in MIX-Co and almost absent in HCP-Co. The model
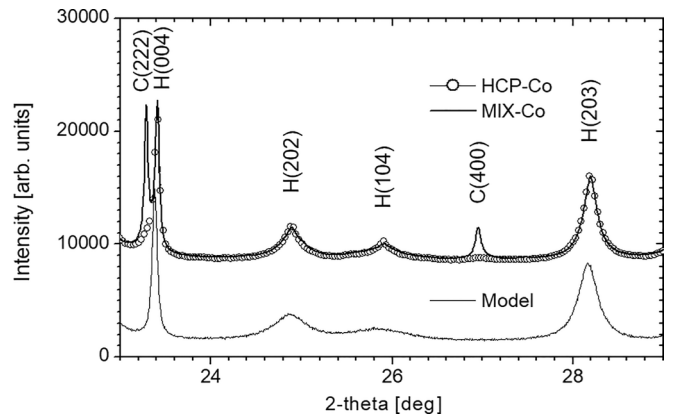

FIG. 3. Selected parts of the SR powder diffraction patterns measured for the MIX-Co (solid line) and HCP-Co (open circles) are shown in upper plots. The only stacking faults insensitive peak is (004) while the remaining peaks are stacking faults sensitive. The SR powder diffraction pattern calculated for a hexagonal model of stacking faults with the probabilities $\alpha_{ST} = 0.0067$ and $\beta_{ST} = 0.03$ (see text) is shown in the lower plot (solid line). The stacking faults sensitive peakshapes calculated with FAULTS using the monoclinic model (not shown) are hard to distinguish from the hexagonal model results. The upper plots were shifted vertically for visualization.

implemented in FAULTS assumes infinitely wide layers with ideal hexagonal planes and the same d-spacing along [001] for both hcp-Co and fcc-Co phases.

F. Analysis of the shapes of stacking-faults' insensitive Bragg peaks

We have analyzed the SR diffraction patterns of the cobalt samples limited to the hcp-Co stacking faults insensitive peaks. The analysis was done in the following steps.

(i) The observed $I(2\theta)$ profiles of insensitive peaks due to the hcp-Co areas and the profiles of separated peaks due to the fcc-Co areas were fitted by the pseudo-Voigt function by using the program WinPlotr [38]. These fits provide the raw values of the integral breadths $\beta_{RAW}(2\theta_{hkl})$, i.e., not corrected for instrumental resolution. The corrected integral breadths are calculated as $\beta(2\theta) = \{\beta_{RAW}(2\theta)^2 - \beta_{NAC}(2\theta)^2\}^{\frac{1}{2}}$, where $\beta_{NAC}(2\theta)$ is interpolated from integral breadths measured with the Na$_2$Ca$_3$Al$_2$F$_{14}$ reference standard [31] [see Fig. 4(c)].

(ii) The resolution corrected integral breadths $\beta(2\theta_{hkl})$ of selected sets of insensitive peaks: [(002);(004);(006)] as well as [(110);(220)] has been analyzed by a Williamson-Hall plot [39] providing information about the average coherent domain size and average microstrain in out-of-plane and in-plane directions.

(iii) The SR powder diffraction patterns limited to insensitive peaks only were analyzed by the Rietveld method by using the program Jana2006 [40] assuming both hexagonal and monoclinic structure models.

The integral breadths of the "insensitive" peaks from hcp-Co and peaks from fcc-Co observed with SR powder diffraction for MIX-Co sample are shown in Fig. 4(a) and for the HCP-Co sample in Fig. 4(b). It was possible to fit the profile of only 3 to 4 peaks due to the fcc-Co phase, especially in the HCP-Co sample where the amount of fcc-Co
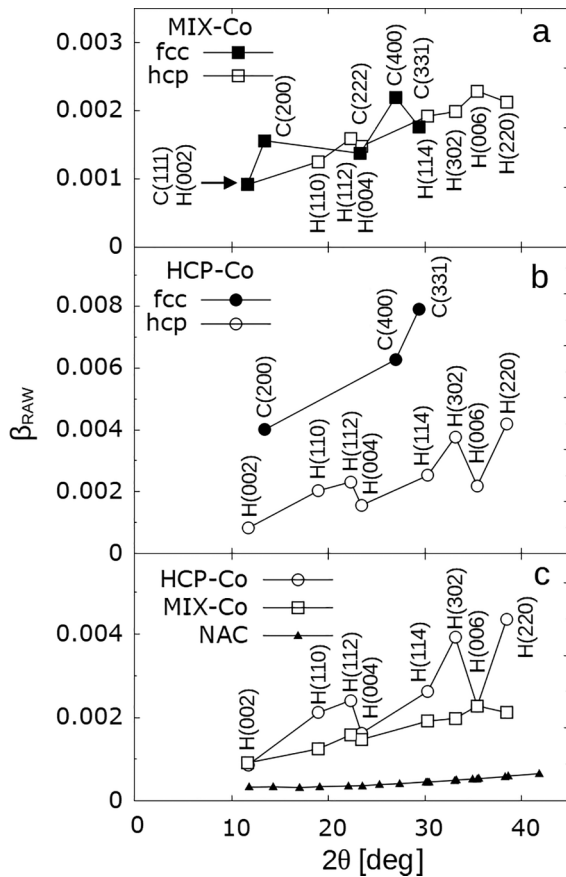
FIG. 4. Integral breadths β_{RAW} (in radians) of the hcp-Co insensitive peaks and fcc-Co peaks observed in the SR diffraction patterns of MIX-Co (a) and HCP-Co (b). The hexagonal and cubic indices are shown. In (c) only the hcp-Co insensitive peaks from MIX-Co and HCP-Co samples are compared with the integral breadths of the $Na_2Ca_3Al_2F_{14}$ reference standard [31] (estimation of the instrumental resolution). Panel (c) is shown to compare the peaks due to the hcp-Co that were already shown in MIX-Co (a) and HCP-Co (b). The lines are shown to guide the eye.

is only 2.5% and the fcc-Co peaks are broad. Figure 4(c) compares the integral breadths of insensitive peaks from hcp-Co observed for MIX-Co and HCP-Co, i.e., it shows the same data as in Figs. 4(a) and 4(b) but without the fcc-Co peaks for easier visualization. The peakwidths of the reference sample for instrumental resolution $Na_2Ca_3Al_2F_{14}$ are shown in Fig. 4(c). Each panel in Figs. 4(a), 4(b), and 4(c) share the same horizontal 2θ scale but the vertical scales are different. The data from panels (a) and (b) is repeated in panel (c) but in a different scale.

The relatively large differences of integral breadths of insensitive $(00l)$ and $(hh0)$ peaks from HCP-Co sample agree with the monoclinic model calculations with the programme FAULTS. The model calculations are compared with experimental data in Fig. 5.

The microstrains (ϵ) and coherent domain sizes (D) are calculated from the observed subset of peaks, which show a linear dependence of their $\beta(2\theta)\cos(\theta)$ vs $\sin\theta$. We use the
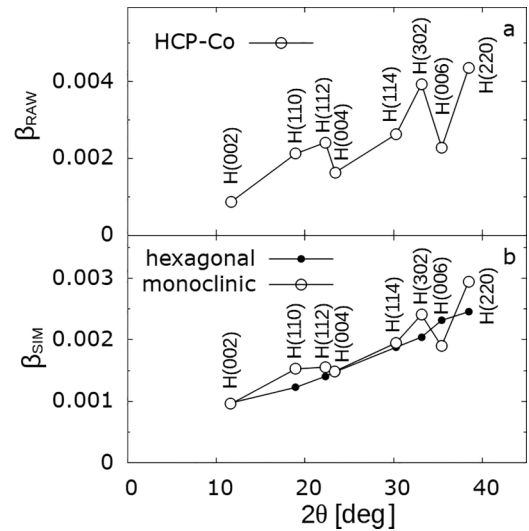

FIG. 5. Observed integral breadths β_{RAW} (in radians) of the hcp-Co insensitive peaks observed in HCP-Co (a) are compared with the results of model calculations with both monoclinic and hexagonal symmetry (b) by the program FAULTS (see text).

Williamson-Hall type linear fit [39],

$$\beta(2\theta)\cos\theta = 4\epsilon\sin\theta + \frac{K\lambda}{D} = A\sin\theta + B, \qquad (5)$$

so the microstrain and the coherent domain size are given by

$$\epsilon = \frac{A}{4} \quad D = \frac{K\lambda}{B}, \qquad (6)$$

where A and B are linear function parameters from Williamson Hall fit and K is the Scherrer's constant set to $K = 0.9$ [41].

For the MIX-Co sample, shown in Fig. 4(a) with (fcc:hcp ratio 18%:82%) the integral breadth of the fcc-Co peaks and of hcp-Co insensitive peaks show a similar linear behavior indicating relatively low microstrains in areas with both hcp and fcc order. The Williamson Hall plot gives the microstrain $\epsilon_{hcp}^{MIX} \approx \epsilon_{fcc}^{MIX} = 0.127(4)\%$ and coherent domain size $D_{hcp}^{MIX} \approx D_{fcc}^{MIX} = 670(100)$ Å. This is much more than the average 55 Å of the hcp-type areas estimated with the programme FAULTS in Sec. III E. This is due to stacking fault insensitive peaks being obtained by summing over multiple hcp-Co and fcc-Co domains in each crystallite as explained in Sec. III B.

The observed linear increase of integral breadths with small slope indicates that both hcp-Co and fcc-Co areas are less strained in the MIX-Co sample than in the HCP-Co sample.

For the HCP-Co sample shown in Fig. 4(b) the situation is different. The integral breadths of the fcc-Co peaks are large, as compared with the fcc-Co peaks from MIX-Co sample, and they show a steep increase vs 2θ indicating larger microstrains. A Williamson-Hall fit for the fcc-Co peaks gives the microstrain $\epsilon_{fcc}^{HCP} = 0.73(4)\%$ and coherent domain size $D_{fcc}^{HCP} = 500(60)$ Å.

The peakwidths of insensitive peaks of the hcp-Co phase do not show a linear $\sin\theta$ behavior, but there are considerable
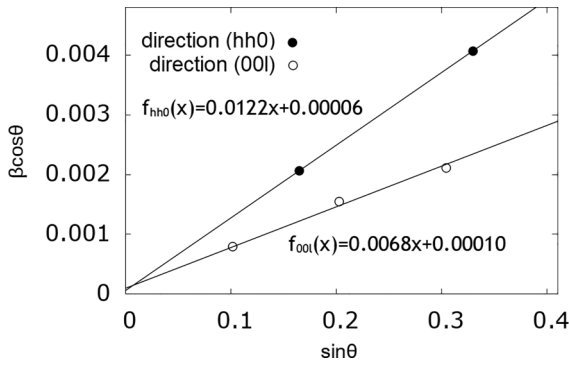
FIG. 6. Williamson-Hall plots for (00*l*) and (*hh*0) peak families of the HCP-Co sample. Formulas of linear functions obtained through least squares method for (00*l*) peaks and linear extrapolation for (*hh*0) peaks are shown in the plot and are expressed in the unit of degrees.

hkl-dependent differences. The (00*l*) group of peaks are narrow indicating a low microstrain and large coherent diffracting domains along the hexagonal direction [001]. The group of broader (*hh*0) peaks indicate larger microstrains within the hexagonal layer (001) planes. The widths of the peaks indexed as (*hh*0) provide the average over three equivalent directions in the (001) plane, i.e., $\pm(h, h, 0); \pm(2h, \bar{h}, 0)$, and $\pm(h, 2\bar{h}, 0)$. The out-of-plane layers' spacing is more regular than the in-plane atomic arrangement inside the hexagonal layers.

In order to quantitatively describe the observed peak broadening of the insensitive peaks from SR diffraction patterns we have performed a Williamson-Hall plot analysis [39] for the group of narrower (00*l*) peaks and the group of broader (*hh*0) peaks. The Williamson-Hall plot for the HCP-Co sample is shown in Fig. 6. The slope of the obtained lines is substantially larger for the (*hh*0) than for the (00*l*), i.e., the in-plane microstrain is larger than in the perpendicular [00*l*] direction. The y-intercept values for fitted lines are very close to zero corresponding to large coherent domain sizes in both directions.

Equations (6) were used for a fit for the three points of the (00*l*) family and for a solution of the set of two linear equations for the two points (110) and (220). In both cases one obtains values of A_{hkl} and B_{hkl} with their uncertainties. The final values are $\epsilon_{00l} = 0.171(5)\%$, $\epsilon_{hh0} = 0.305(7)\%$, $D_{00l} = 3900(1000)$ Å, and $D_{hh0} = 6600(2000)$ Å for HCP-Co. The estimated crystallite sizes have large uncertainties but the difference of microstrains ϵ_{00l} and ϵ_{hh0} is significant.

G. Temperature dependence of the hcp-Co and fcc-Co lattice parameters

The SR powder diffraction patterns of HCP-Co and MIX-Co samples at RT and the MIX-Co sample measured at temperatures between RT and 250 °C have been analyzed using Rietveld refinement [42,43] by using the program Jana2006 [40]. For the hcp-Co phase only the insensitive Bragg peaks were used in the refinement. The hcp-Co phase [hexagonal space group $P6_3/mmc$ and Co atoms at position (2c)] and the fcc-Co phase [cubic space group $Fm\bar{3}m$ and Co atoms at position (4a)] were assumed in the refinements. The

refinement was satisfactory and the resulting hexagonal a_h, c_h and cubic a_c lattice parameters are presented in Table I. The interlayer d spacing equals $d_{hcp} = c_h/2$ and $d_{fcc} = a_c/\sqrt{3}$ in hcp-Co and fcc-Co, respectively. The relative difference of interlayer spacing,

$$\left(\frac{\Delta d}{d}\right)_\perp = \frac{d_{fcc} - d_{hcp}}{d_{hcp}} = \frac{2a_c}{\sqrt{3}c_h} - 1, \quad (7)$$

where $\perp$ indicates perpendicular to the layers, was reported in early works on cobalt to be equal 0.57% [34], 0.55% [33], and 0.48% [35] at RT, i.e., not far from our values, i.e., 0.488(5)% for MIX-Co and 0.614(5)% for HCP-Co, see Table I. The values of $(\Delta d/d)_\perp$ decrease with temperature as shown in Table I. The nearest-neighbor in-plane distance is equal $l_{hcp} = a_h$ and $l_{fcc} = a_c/\sqrt{2}$ in hcp-Co and fcc-Co, respectively. The relative difference of nearest-neighbor in-plane distances is calculated as

$$\left(\frac{\Delta d}{d}\right)_\parallel = \frac{l_{fcc} - l_{hcp}}{l_{fcc}} = 1 - \sqrt{2}\frac{a_h}{a_c}, \quad (8)$$

where $\parallel$ indicates parallel to the layers' surface, is also shown in Table I.

The lattice constants observed for both hcp and fcc areas in the HCP-Co and MIX-Co samples differ. Please note that the fcc-Co (occupying only 2.5% in the HCP-Co sample) is highly strained, as shown by broad peaks in Fig. 4(b) and the interlayer misfit $(\Delta d/d)_\perp$ is larger than in the MIX-Co sample (where the fcc-Co occupies 18%).

The temperature dependence of both hexagonal $a_h(T)$, $c_h(T)$ and cubic $a_c(T)$ lattice parameters is linear as shown, e.g., in [1,35] and their relative differences, e.g., $(\Delta d/d)_\perp$ and $(\Delta d/d)_\parallel$ tend linearly towards zero with temperature (see Table I, plot not shown), i.e., at higher temperatures the misfits try to relax. The relative difference of interlayer distances in hcp-to-fcc cobalt $(\Delta d/d)_\perp$ was reported earlier, e.g., [33–35] while the much smaller $(\Delta d/d)_\parallel$ intralayer distance difference values were not reported so far for cobalt, to the best of our knowledge.

H. The monoclinic and hexagonal models of the crystal structure of hcp-Co

The hkl-selective peak broadening of insensitive peaks shown in Fig. 4 can be explained by a monoclinic deformation of the crystal lattice. This is consistent with the magnetic spin reorientation effect reported in hcp-Co single crystal [18,19]. We tried to verify this hypothesis by performing Rietveld analysis of the SR diffraction patterns by using the program Jana2006 [40] with only insensitive peaks included. The H(002) and C(111) peaks were excluded from the refinements due to overlap.

The usual hexagonal close-packed structure (space group $P6_3/mmc$) will be denoted as "undistorted" and the monoclinic (space group $C2/m$) as "distorted". The lattice parameters and unit-cell vectors of undistorted and distorted hcp-Co will be denoted with superscripts 0 and 1, respectively.

The hcp-Co structure can be described in the hexagonal space group $P6_3/mmc$ with the generators in Seitz notation: $\{3_{001}^+|000\}$, $\{2_{001}|00\frac{1}{2}\}$, $\{2_{110}|000\}$, $\{\bar{1}|000\}$. If we remove the two rotations around [001]: $\{3_{001}^+|000\}$ and $\{2_{001}|00\frac{1}{2}\}$ we

TABLE I. Values of lattice constants of the hcp-Co and fcc-Co phases determined from SR powder diffraction measurements on the HCP-Co and MIX-Co samples at different temperatures. The relative differences of out-of-plane [Eq. (7)] and in-plane distances [Eq. (8)] is also shown.

Sample	temp. [°C]	a_h [Å]	c_h [Å]	c_h/a_h	a_c [Å]	$(\Delta d/d)_\perp$ [%]	$(\Delta d/d)_\parallel$ [%]
HCP-Co	25	2.50760(6)	4.07350(16)	1.62446(7)	3.5494(12)	0.614(36)	+0.088(35)
MIX-Co	25	2.50811(6)	4.07432(16)	1.62446(7)	3.54568(12)	0.488(5)	−0.037(4)
MIX-Co	100	2.51099(5)	4.08039(13)	1.62501(6)	3.54989(11)	0.458(4)	−0.034(4)
MIX-Co	150	2.51269(5)	4.08406(14)	1.62537(6)	3.55235(12)	0.437(5)	−0.032(4)
MIX-Co	200	2.51445(5)	4.08783(13)	1.62574(6)	3.55491(12)	0.416(5)	−0.030(4)
MIX-Co	250	2.51632(5)	4.09181(14)	1.62611(6)	3.55765(13)	0.396(5)	−0.027(4)

obtain the set of generators of the monoclinic space group $C2/m$. The group-subgroup relation between $P6_3/mmc$ and $C2/m$ gives the following relations between the hexagonal unit cell vectors: $\mathbf{a}_h^0$, $\mathbf{b}_h^0$, and $\mathbf{c}_h^0$ and the monoclinic unit-cell vectors $\mathbf{a}_m^0$, $\mathbf{b}_m^0$, and $\mathbf{c}_m^0$,

$$\mathbf{a}_m^0 = \mathbf{b}_h^0 - \mathbf{a}_h^0, \tag{9a}$$

$$\mathbf{b}_m^0 = \mathbf{b}_h^0 + \mathbf{a}_h^0, \tag{9b}$$

$$\mathbf{c}_m^0 = \mathbf{c}_h^0, \tag{9c}$$

where the subscripts "h" and "m" refer to the hexagonal and monoclinic settings, respectively. The Co atoms are located at the sites (2c) [point group $\bar{6}m2$] of the space group $P6_3/mmc$: at $(\frac{1}{3}, \frac{2}{3}, \frac{1}{4})$ and $(\frac{2}{3}, \frac{1}{3}, \frac{3}{4})$. In the monoclinic symmetry the Co atoms are at the site (4i) [point group m] of the $C2/m$ space group. This site has two free positional parameters x, z and the atoms are located at: $(x, 0, z)$, $(\bar{x}, 0, \bar{z})$, $(\frac{1}{2} + x, \frac{1}{2}, z)$, $(\frac{1}{2} - x, \frac{1}{2}, \bar{z})$. In all Rietveld refinements these parameters were fixed at $x = 2/3$ and $z = 1/4$ to match exactly the coordinates of the hexagonal structure. Please note that the insensitive peaks cannot be used to determine x and z, see Eqs. (4a) and (4b).

In order to compare easier the undistorted hexagonal structure and the distorted monoclinic structure we will use the pseudohexagonal setting of the monoclinic structure. The pseudohexagonal vectors $\mathbf{a}_h^1$, $\mathbf{b}_h^1$, and $\mathbf{c}_h^1$ can be obtained by taking reverse transformation of Eqs. (9a)–(9c) and changing all the superscripts from 0 to 1,

$$\mathbf{a}_h^1 = \frac{1}{2}(\mathbf{b}_m^1 - \mathbf{a}_m^1), \tag{10a}$$

$$\mathbf{b}_h^1 = \frac{1}{2}(\mathbf{b}_m^1 + \mathbf{a}_m^1), \tag{10b}$$

$$\mathbf{c}_h^1 = \mathbf{c}_m^1. \tag{10c}$$

The pseudohexagonal lattice parameters fulfill the following equations:

$$a_h^1 = b_h^1, \tag{11a}$$

$$\alpha_h^1 + \beta_h^1 = 180°, \tag{11b}$$

which can be derived by calculating scalar products $\mathbf{a}_h^1\mathbf{a}_h^1$, $\mathbf{b}_h^1\mathbf{b}_h^1$ as well as $\mathbf{a}_h^1\mathbf{c}_h^1$ and $\mathbf{b}_h^1\mathbf{c}_h^1$ using Eqs. (10a)–(10c). Please note that the pseudohexagonal setting is a primitive cell choice for base-centered monoclinic structures. The relations between lattice constants in monoclinic and pseudohexagonal

settings of the distorted structure, derived from Eqs. (10a)–(10c) are given by

$$a_h^1 = b_h^1 = \frac{1}{2}\sqrt{(a_m^1)^2 + (b_m^1)^2}, \tag{12a}$$

$$c_h^1 = c_m^1, \tag{12b}$$

$$\cos\alpha_h^1 = \cos(\pi - \beta_h^1) = \frac{a_m^1 \cos\beta_m^1}{\sqrt{(a_m^1)^2 + (b_m^1)^2}}, \tag{12c}$$

$$\cos\gamma_h^1 = \frac{(b_m^1)^2 - (a_m^1)^2}{(b_m^1)^2 + (a_m^1)^2}. \tag{12d}$$

The mutual arrangement of the hexagonal, pseudohexagonal, and monoclinic axes is shown in Fig. 7. The distortions from hexagonal symmetry of the hcp-Co areas are expected to be small because the variation of the peakwidths shown in Fig. 4 are also relatively small. It can be assumed that with three small distortion parameters, which fulfill $\frac{\delta\alpha}{\alpha} \ll 1$, $\frac{\delta\gamma}{\gamma} \ll 1$ and $\frac{\delta a}{a} \ll 1$, we get
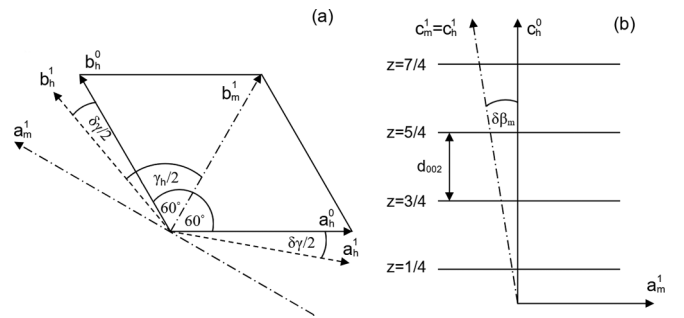
$$a_h^1 = b_h^1 = a_h^0 + \delta a, \tag{13a}$$

FIG. 7. The hexagonal ($\mathbf{a}_h^0$, $\mathbf{b}_h^0$, $\mathbf{c}_h^0$) pseudohexagonal ($\mathbf{a}_h^1$, $\mathbf{b}_h^1$, $\mathbf{c}_h^1$), and monoclinic ($\mathbf{a}_m^1$, $\mathbf{b}_m^1$, $\mathbf{c}_m^1$) axes shown in two projections (a) perpendicular to the hexagonal $\mathbf{c}_h^*$ reciprocal lattice vector and (b) perpendicular to the monoclinic $\mathbf{b}_m^*$ reciprocal lattice vector. The $z = 1/4$, 3/4... are the coordinates of atomic planes and they are the same in all three settings. Solid lines mark the base of the hexagonal unit cell and hexagonal axes, dashed lines are used for the pseudohexagonal vectors, and the dashed-dotted lines denote the monoclinic axes. The $\delta\gamma/2$ and $\delta\beta_m$ angles were significantly enlarged for visualization. The distance between adjacent planes is denoted as d_{002} in (b) with the same 002 indices in all three settings.

TABLE II. Lattice constants and angles refined from the SR powder diffraction pattern of the HCP-Co sample using only "insensitive" peaks (see text) using Rietveld method with use of the hexagonal (column 1) and monoclinic (columns 2 and 5) models. In the hexagonal model Co atoms are at positions (2c) of $P6_3/mmc$ while in monoclinic model in positions (4i) of $C2/m$ (for details see Sec. III H). The refinement quality indicators wRp are given in the bottom row. The results of refinements for the best monoclinic model with both $\delta\alpha \neq 0$ and $\delta\gamma \neq 0$ (see text) are shown in both pseudohexagonal (column 4) and monoclinic (column 5) settings.

No.	1	2	3	4	5
Model	Hex $P6_3/mmc$	Ps-hex $\alpha-$fix $\gamma-$free	Ps-hex $\alpha-$free $\gamma-$fix	Ps-hex $\alpha-$free $\gamma-$free	Mono C2/m
a [Å]	2.50807(10)	2.50946(11)	2.50828(10)	2.50973(10)	4.34924(22)
b [Å]	$= a$	$= a$	$= a$	$= a$	2.50578(11)
c [Å]	4.07431(17)	4.07416(16)	4.07455(16)	4.07474(15)	4.07474(15)
α [°]	90	90	90.1247(33)	90.1115(29)	90
β [°]	90	90	89.8753(33)	89.8884(29)	90.1287(32)
γ [°]	120	120.1090(33)	120	120.1036(32)	90
wRp [%]	10.71	10.02	9.82	9.11	9.11

$$c_h^1 = \frac{c_h^0}{\sin(90° + \delta\alpha)} = c_h^0 + O(\delta\alpha^2) \approx c_h^0, \quad (13b)$$

$$\alpha_h^1 = 90° + \delta\alpha, \quad (13c)$$

$$\beta_h^1 = 90° - \delta\alpha, \quad (13d)$$

$$\gamma_h^1 = 120° + \delta\gamma. \quad (13e)$$

The pseudohexagonal angle α_h^1 between $\mathbf{c}_h^1$ and $\mathbf{b}_h^1$ is equal to $(90° + \delta\alpha)$ and it means that $\delta\alpha$ is a measure of the inclination of the former hexagonal [001] axis with respect to the lines of atoms arranged along $\mathbf{b}_h^1$ in the former hexagonal layer. On the other hand the pseudohexagonal angle $\gamma_h^1 = 120° + \delta\gamma$ describes a deformation of the atomic layer itself.

I. Rietveld refinements of SR diffraction patterns of hcp-Co assuming the monoclinic symmetry

In the first step of Rietveld refinements, the undistorted hexagonal crystal structure described by the space group $P6_3/mmc$ was used, giving a relatively good refinement quality parameter wRp, see Table II (column 1) for HCP-Co sample and Table III (column 1) for MIX-Co sample. In the next steps, the monoclinic crystal structure with the monoclinic symmetry (space group $C2/m$) was used. For better visibility of data presentation we have used the pseudohexagonal setting defined by Eqs. (10a)–(12d). The model assuming a deformed (NON-hexagonal) layers, which are perpendicular to the hexagonal [001] axis, i.e., $\alpha = \beta = 90°$ and $\gamma = 120° + \delta\gamma$ is shown in column 2 of Table II and Table III. The model assuming hexagonal layers, which are NOT perpendicular to the hexagonal [001] axis, i.e., $\alpha = 90° + \delta\alpha$, $\beta = 90° - \delta\alpha$, and $\gamma = 120°$ is shown in column 2 of Table II and Table III. Both these models give better agreement than the hexagonal one. The best agreement is obtained for the model of NON-hexagonal layers, which are NOT perpendicular to the hexagonal axis, i.e., $\delta\alpha \neq 0$ and $\delta\gamma \neq 0$, as shown in columns 4 and 5 of Table II. These two columns refer to the same model given in pseudohexagonal and monoclinic settings, respectively. For better visualization the wRp minimum as a function of the angular deviations $\delta\alpha$ and $\delta\gamma$ is shown with the color map in Fig. 8. The color map shows the results of 100 refinements with fixed values of $\delta\alpha$ and $\delta\gamma$.

TABLE III. Lattice constants and angles refined from the SR powder diffraction pattern of the MIX-Co sample using only "insensitive" peaks (see text) using Rietveld method with use of the hexagonal (column 1) and monoclinic (columns 2 and 5) models. In the hexagonal model Co atoms are at positions (2c) of $P6_3/mmc$ while in monoclinic model in positions (4i) of $C2/m$ (for details see Sec. III H). The refinement quality indicators wRp are given in the bottom row of the table. The results of refinements for the best monoclinic model with both $\delta\alpha \neq 0$ and $\delta\gamma \neq 0$ (see text) are shown in both pseudohexagonal (column 4) and monoclinic (column 5) settings.

| No.	1	2	3	4	5
Model	Hex $P6_3/mmc$	Ps-hex $\alpha-$fix $\gamma-$free	Ps-hex $\alpha-$free $\gamma-$fix	Ps-hex $\alpha-$free $\gamma-$free	Mono C2/m
a [Å]	2.50806(5)	2.50898(7)	2.50812(6)	2.50889(8)	4.34671(17)
b [Å]	$= a$	$= a$	$= a$	$= a$	2.50682(18)
c [Å]	4.07451(15)	4.07453(14)	4.07446(15)	4.07467(15)	4.07467(15)
α [°]	90	90	90.0939(33)	90.0804(36)	90
β [°]	90	90	89.9061(33)	89.9196(29)	90.0928(37)
γ [°]	120	120.0732(33)	120	120.0544(43)	90
a_c [Å]	3.54565(12)	3.54577(11)	3.54548(11)	3.54567(11)	3.54567(11)
wRp[%]	15.83	15.35	15.09	14.95	14.95
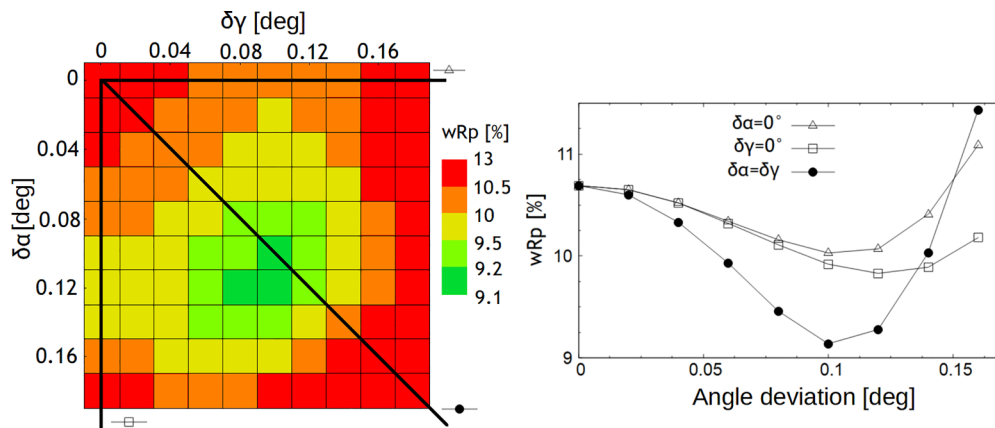
FIG. 8. (Left panel) Values of the fit quality indicator, wRp vs angular deviations $\delta\alpha$ and $\delta\gamma$ obtained for the HCP-Co sample. (Right panel) Plot of the one-dimensional cuts with the value of wRp along the lines: $\delta\alpha = 0 (\triangle)$; $\delta\gamma = 0 (\square)$; $\delta\alpha = \delta\gamma (\bullet)$. The angle deviation is $\delta\gamma$ for $(\triangle)$, $\delta\alpha$ for $(\square)$ and $\delta\alpha = \delta\gamma$ for $(\bullet)$.

The refined angular distortion parameters $\delta\alpha = 0.111(3)°$ and $\delta\gamma = 0.104(4)°$ are larger than their statistical errors and this result supports the hypothesis of a monoclinic distortion of the averaged crystal structure of the hcp-Co areas.

J. Neutron diffraction studies of the spin reorientation in the hcp areas of cobalt

The monoclinic symmetry proposed above is compatible with the magnetic phenomena: the ferromagnetic ordering of hcp-Co can be described by the magnetic space group $C2'/m'$. This space group allows a continuous ferromagnetic spin reorientation, as discussed, e.g., in [44]. The Co atoms are allowed to have a ferromagnetically ordered magnetic moments: $\mathbf{M} = [M_x^0, 0, M_z^0]$, i.e., in the plane perpendicular to the unique monoclinic axis $\mathbf{b}_m^1$. It means that the ferromagnetic ordering is described in monoclinic symmetry with the magnetic mode F0F instead of a 00F mode in hexagonal symmetry as explained in [23]. The gradual spin reorientation by any angle is possible in agreement with magnetization [17] and neutron diffraction results, e.g., [18,19].

In the neutron diffraction study with instrument D2B we tried to determine the direction of the Co magnetic moments at RT. We performed Rietveld refinement using only the peaks insensitive to the stacking faults, similarly as with SR diffraction data described earlier. The neutron diffraction pattern contains only four insensitive peaks—(002), (110), (112), and (004) thus limiting the information we can extract with this approach.

In order to refine the direction of the magnetic moments we used the $P\bar{1}$ magnetic space group instead of the space group $P6_3/mmc$. The lattice constants were constrained $a = b$ and the angles $\alpha = \beta = 90°$, $\gamma = 120°$ were fixed. The atoms were placed at $(\frac{1}{3}, \frac{2}{3}, \frac{1}{4})$ and $(\frac{2}{3}, \frac{1}{3}, \frac{3}{4})$ positions with an initial magnetic moment along the c-axis. The unit cell has the same metric as the hexagonal one, but the magnetic space group allows any direction of the magnetic moment. After obtaining a stable solution we started to gradually change the polar angle ϕ_m between the magnetic moment and the hexagonal c axis and we refine the magnetic moment length and the Debye-Waller factor keeping the angle ϕ_m fixed for each of

the refinements. The resulting refinement with $\phi_m = 10°$ is shown in Fig. 9. The unfavourable values of the scattering lengths b(coh) and b(inc) seriously limit the possibilities of neutron diffraction studies of cobalt.

The results of refined magnetic moment vs ϕ_m and the refinement quality indicator wRp are shown in Fig. 10. With the neutron powder diffraction data one can determine the magnetic moment direction with an accuracy of about $\pm 10°$. Our fit gives a value of the Co magnetic moment $0.86(5)\mu_B$. Earlier studies by Bertaut *et al.* [19] reported a value of $\langle S^2 \rangle = 0.703 \, \mu_B^2$ at 236 °C. For RT one can expect a magnetic moment larger by a few percent than $\sqrt{0.703}\mu_B = 0.84\mu_B$, which is close to our refined value. The wRp parameter is changing slightly with the direction of the magnetic moment. There is an anticorrelation: for increasing ϕ_m the value of U_{iso} decreases while M_{tot} increases. In fact we use four magnetic and stacking-faults-insensible peaks only (see Fig. 9), so this is not enough to obtain a reliable value of both M_{tot} and the Debye-Waller factor U_{iso}. SR powder diffraction peaks give U_{iso} values about 0.01 Å² but these are obtained with a fit using about 10 peaks and we cannot compare them with U_{iso} obtained from neutron diffraction in Fig. 10. Fits with
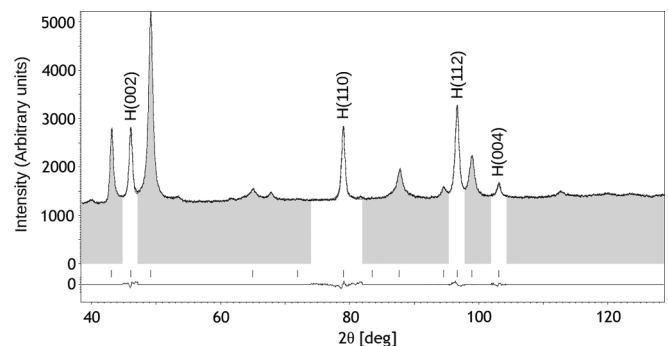

FIG. 9. Neutron powder diffraction pattern of HCP-Co sample measured with instrument D2B at RT. The refinement was done with the four peaks "insensitive" to stacking faults (see text). The grey sections were excluded from refinements. The difference curve is shown at the bottom.
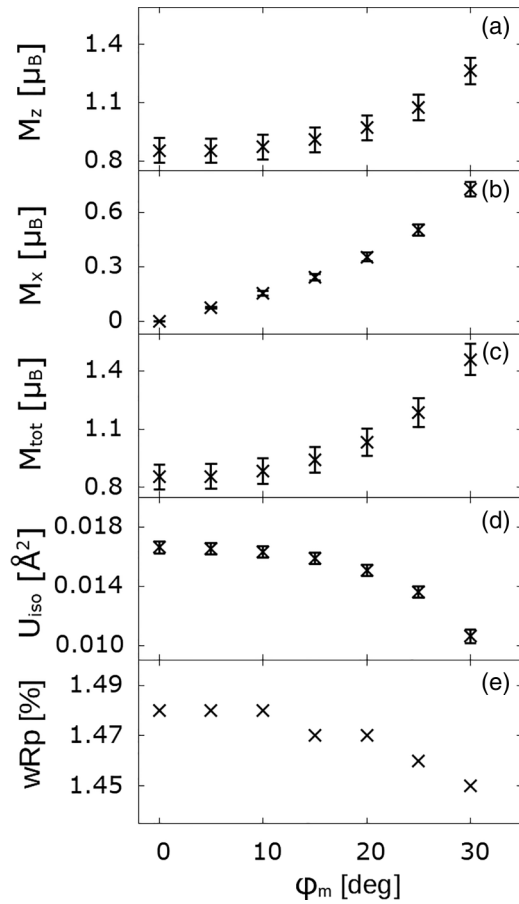
FIG. 10. The values of refined magnetic moment in directions parallel (a) and perpendicular (b) to hexagonal c axis vs the angle ϕ_m between spin direction and the c axis. [(c)–(e)] Show the total magnetic moment, the isotropic displacement factor U_{iso} and the refinement quality indicator wRp.

the monoclinic symmetry were not successful because of the limited number of insensitive peaks in the neutron diffraction pattern.

In the neutron diffraction study with instrument SPODI we tried to study the spin-reorientation process in hcp-Co. The measurements with HCP-Co sample at SPODI started with an unexpected effect. After the first measurements at RT the temperature was increased to 380 °C in order to go surely above the spin reorientation transition. Unfortunately at this high temperature the metastable hcp phase started to decompose and about 15% of the sample volume changed irreversibly from hcp to fcc. This transition took place in a relatively short time of a few minutes. Next, the temperature was reduced to 330 °C and the measurements were run in the cycle by cooling in steps from 330 °C down to 100 °C and next by warming in steps up to 330 °C. At the end the sample was cooled down and the measurement at RT was repeated. The amount of fcc-to-hcp content did not change during the cycling between 330 °C and 100 °C.

The statistical accuracy accessible in the temperature-dependent measurements at SPODI was not enough to determine the magnetic moments direction with a precision better than $\pm 10°$. In order to visualize the main effects we

show the measured temperature dependence of the (002) and (100) Bragg peaks in Figs. 11(a) and 11(b), respectively. These Bragg peaks contain both nuclear and magnetic contributions. The (002) peak is insensitive, while the (100) has contributions due to the stacking faults, see e.g., Fig. 2. The present results are compared with results from Bertaut *et al.* [18] for (002) in Figs. 11(a) and 11(c) respectively, while for (100) in Figs. 11(b) and 11(d), respectively. Both experiments show a gradual change of the intensity ratios, which can be interpreted as a sign of a spin reorientation in the Co single crystal [18] across about $\Delta T = 80$ °C while in powder HCP-Co the spin-reorientation starts at about 100 °C, and finishes around 300 °C, see Fig. 11.

From our neutron powder diffraction data we can confirm that there is a spin-reorientation process in our powder HCP-Co sample, but the process takes place in a wider temperature range than in the single crystal as reported by Bertaut *et al.* [18,19]. It is, however, not possible to confirm if the magnetic moments are exactly parallel to the hexagonal [001] at 100 °C nor exactly perpendicular to [001] above 300 °C. It was also not possible to confirm or refute the hypothesis of the monoclinic symmetry of the averaged crystal structure of hcp-Co ordered areas using the neutron powder diffraction data from D2B and SPODI.

K. Model of the atomic layers in monoclinic (pseudohexagonal) hcp-Co phase model

Let us look at the nearest-neighbor interatomic distances in the monoclinic lattice of the hcp-Co phase model. A schematic plot of the monoclnic (formerly: hexagonal, now pseudohexagonal) A and B layers is given in Fig. 12. The atoms in the A layer $A_0, ...A_6$ are located in the drawing plane, i.e., at $z = 1/4$: A_0 at $(0, 0, \frac{1}{4})$, A_1 at $(1, 1, \frac{1}{4})$, A_2 at $(0, 1, \frac{1}{4})$, and so on. The atoms in the B layer (left panel) are located at $z = -1/4$, i.e., below the A layer at $B_1(\frac{1}{3}, -\frac{1}{3}, -\frac{1}{4})$, $B_2(\frac{1}{3}, \frac{2}{3}, -\frac{1}{4})$, $B_3(-\frac{2}{3}, -\frac{1}{3}, -\frac{1}{4})$. The atoms in the C layer (right panel) are located at $z = 3/4$, i.e., above the A layer at $C_1(-\frac{1}{3}, \frac{1}{3}, \frac{3}{4})$, $C_2(-\frac{1}{3}, -\frac{2}{3}, \frac{3}{4})$, $C_3(\frac{2}{3}, \frac{1}{3}, \frac{3}{4})$. C_i is the image of B_i by inversion centered at A_0. The hexagonal and pseudohexagonal coordinate systems defined by vectors $(\mathbf{a}_h^0, \mathbf{b}_h^0, \mathbf{c}_h^0)$ and $(\mathbf{a}_h^1, \mathbf{b}_h^1, \mathbf{c}_h^1)$ [see Eqs. (9) and (10)] have the same common origin, see also Fig. 7. The unique monoclinic axis $\mathbf{b}_m^1 = [010]_m$ is parallel to both,

$$\mathbf{b}_m^1 \parallel \left(\mathbf{a}_h^0 + \mathbf{b}_h^0\right) \parallel \left(\mathbf{a}_h^1 + \mathbf{b}_h^1\right) \tag{14}$$

as shown in Fig. 12 with the dashed line. The unique monoclinic plane $(010)_m$ is drawn with the dash-dotted line. We assume that the fractional atomic coordinates of all atoms in A, B, and C layers remain constant. We consider the difference in atomic positions between the hexagonal and pseudohexagonal structure models due to a change of the crystallographic axes as given by Eqs. (9) and (10). In Fig. 12 it is assumed that the lengths of the hexagonal and pseudohexagonal lattice parameters are the same, i.e., $a_h^0 = b_h^0 = a_h^1 = b_h^1$ and $c_h^0 = c_h^1$ but the pseudohexagonal angles change from $90°$ and $120°$. The pseudohexagonal $\mathbf{c}_h^1$ axis rotates within the unique monoclinic plane towards atom B_1 in Fig. 12, see also Eqs. (9) and (10) with Fig. 7. In the refined structural model for hcp-Co the pseudohexagonal angles α, β, and γ change by about
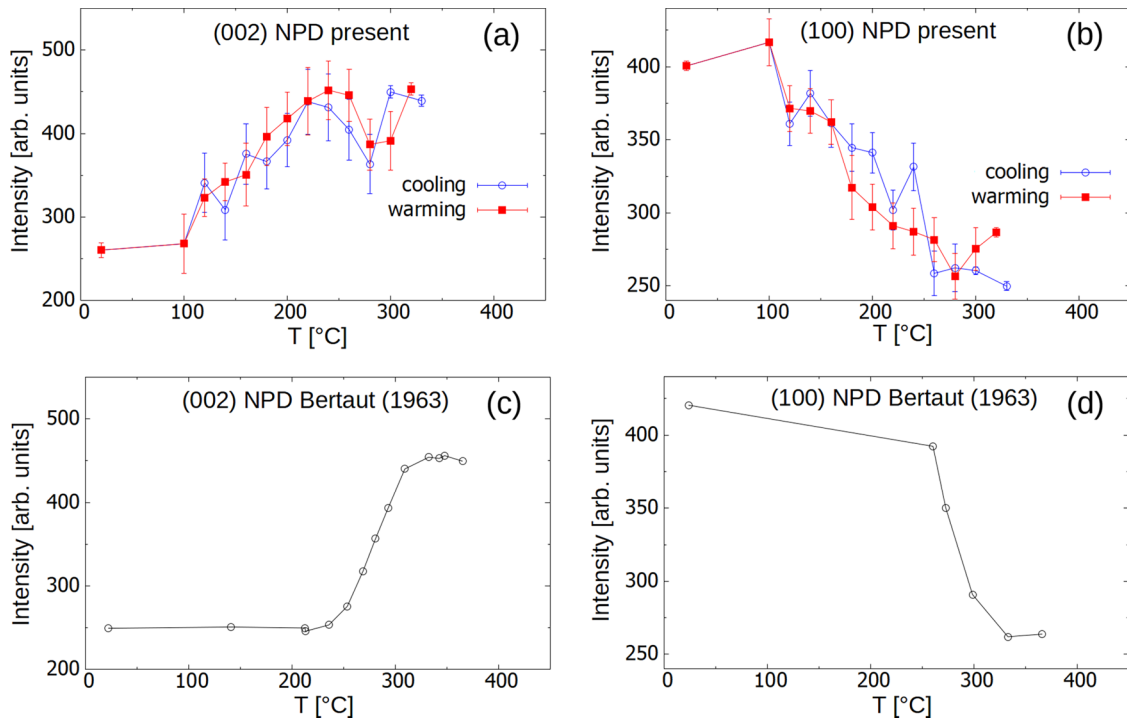
FIG. 11. Temperature dependence of the Bragg peaks measured with neutron diffraction for powder HCP-Co sample in the present study using instrument SPODI peak (002) (a) and peak (100) (b). Similar results obtained from neutron diffraction on a Co single crystal by Bertaut *et al.* [18,19] are shown: peak (002) (c) and (100) (d).

$0.11°$ and it is hardly visible on a drawing. For visualization purposes, Fig. 12 is drawn with $\delta\alpha$, $\delta\beta$, and $\delta\gamma$ about $10°$. The shifts of the atomic positions are shown with arrows. Please note that the shifts have also a small vertical component whose sign is given as $+$ or $-$ in Fig. 12.

The distance from A_0 to neighbor atoms within the monoclinic plane, $d(A_0B_1) = d(A_0C_1)$ are different from the distances to the atoms outside this plane, $d(A_0B_2) = d(A_0B_3) = d(A_0C_2) = d(A_0C_3)$. In the usual way of explaining the partial dislocation in the hcp-fcc boundary region, see e.g., [14,15], each atom from the A layer has three equivalent neighbors in the B layer and three equivalent neighbors in the C layer. If the pseudohexagonal system proposed here describes the hcp-Co and fcc-Co domains then there may be a preference for the partial dislocation to be directed either along the monoclinic axis or within the monoclinic plane. If the proposed monoclinic model works, then we can expect that the maximal inclination of the layers with respect to the hexagonal [001] axis occurs within the monoclinic plane, i.e., along the line $C_1 - A_0 - B_1$.

If this model works well, then one can suppose that the maximally inclined layers, may preferentially be directed along the unique monoclinic plane direction (dotted line). This hypothesis could explain why multiple dislocations often choose one preferred direction in the cobalt grain as it was often reported, e.g., in [11,12].

IV. SUMMARY

The present study confirms that the more realistic crystal structure model provides a better description of the observed diffraction data as compared with the simplified model.

The initial hypothesis that the averaged crystal structure of the hcp-Co areas is not hexagonal but monoclinic has been confirmed by SR powder diffraction and neutron diffraction. This is in agreement with the observed temperature driven reorientation [18,19] of the ferromagnetic moments of cobalt. During such a reorientation the magnetic moments should be confined to a plane, which is perpendicular to the unique monoclinic axis, see e.g., [44]. The argument about monoclinic symmetry of crystals with a continuous spin reorientation [44] is valid for single-phase systems. The cobalt crystallites do not fulfill these assumptions because they are not single phase.
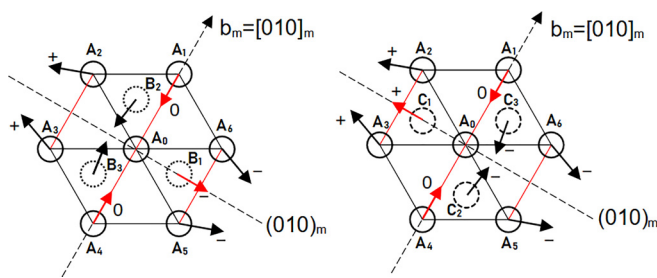

FIG. 12. Schematic presentation of the arrangement of atoms seen from top of the A and B layers (left panel) and A and C layers (right panel). The Co atoms represented by open circles (A, solid lines; B, dotted lines; and C, dashed lines) are shown at their positions in the hexagonal lattice. The vectors indicate how these atoms move on changing to the pseudohexagonal, i.e., monoclinic crystal structure model. The symbol $+$ or 0 or $-$ next to the vector shows if the vector points below or above (see text). The unique monoclinic axis $\mathbf{b}_m^1$ (dash-dotted line) and the monoclinic plane $(010)_m$ (dotted line) are shown.

Besides the symmetry of the crystal structure, there are interesting observations related to the microstrains. Both MIX-Co sample (fcc:hcp = 18%:82%) and HCP-Co sample (fcc:hcp = 2.5%:97.5%) show broad stacking-faults-sensitive hcp-Co peaks with very similar shapes for both samples, see Fig. 3. The remaining peaks, which are (nominally) insensitive to stacking faults show considerably different widths for both samples, see Fig. 4. It means that the two samples have a different distribution of microstrains. Surprisingly, the MIX-Co sample shows both hcp-Co and fcc-Co with low microstrains $\epsilon \approx 0.13\%$, while the HCP-Co sample shows large microstrains for the fcc-Co: $\epsilon \approx 0.73\%$ and hcp-Co: $\epsilon_{hh0} \approx 0.30\%$ (along [110]) and $\epsilon_{00l} \approx 0.17\%$ (along [001]). It means that the presence of a smaller amount of the fcc-Co areas induces larger microstrains in the hcp-Co areas.

Besides the different fcc contents and different microstrains both MIX-Co and HCP-Co samples show similar monoclinic lattice parameters and similar type of stacking faults. These observations show the need for a revisit of the quantitative models of stacking faults in cobalt.

[1] T. Nishizawa and K. Ishida, The Co (cobalt) system, Bull. Alloy Phase Diagrams **4**, 387 (1983).

[2] O. S. Edwards and H. Lipson, Imperfections in the structure of cobalt. I. Experimental work and proposed structure, Proc. R. Soc. London A **180**, 268 (1942).

[3] A. J. C. Wilson, Imperfections in the structure of cobalt. II. Mathematical treatment of proposed structure, Proc. R. Soc. London A **180**, 277 (1942).

[4] H. Jagodzinski, Eindimensionale Fehlordnung in Kristallen und ihr Einfluss auf die Roentgeninterferenzen. I. Berechnung des Fehlordnungsgrades aus den Roentgenintensitaeten, Acta Crystallogr. **2**, 201 (1949).

[5] H. Jagodzinski, Eindimensionale Fehlordnung in Kristallen und ihr Einfluss auf die Röntgeninterferenzen. II. Berechnung der fehlgeordneten dichtesten Kugelpackungen mit Wechselwirkungen der Reichweite 3, Acta Crystallogr. **2**, 208 (1949).

[6] J. Sort, S. Surinach, J. S. Muñoz, M. D. Baró, M. Wojcik, E. Jedryka, S. Nadolski, N. Sheludko, and J. Nogués, Role of stacking faults in the structural and magnetic properties of ball-milled cobalt, Phys. Rev. B **68**, 014421 (2003).

[7] F. Frey, J. Schneider, W. Prandl, C. Zeyen, and K. Ziebeck, The HCP-FCC transition in pure Co investigated by neutron scattering, J. Phys. F **9**, 603 (1979).

[8] F. Frey and H. Boysen, Disorder in cobalt single crystals, Acta Crystallogr. Sect. A **37**, 819 (1981).

[9] O. Blaschko, G. Krexner, J. Pleschiutschnig, G. Ernst, C. Hitzenberger, H. P. Karnthaler, and A. Korner, Coherent Modulated Structure during the Martensitic hcp-fcc Phase Transition in Co and in a CoNi Alloy, Phys. Rev. Lett. **60**, 2800 (1988).

[10] A. Delavignette, Dissociation and plasticity of layer crystals, J. Phys. Colloques **35**, C7-181 (1974).

[11] J. W. Christian, A theory of the transformation in pure cobalt, Proc. R. Soc. London A **206**, 51 (1951).

[12] A. Korner and H. P. Karnthaler, Weak-beam study of glide dislocations in h.c.p. cobalt, Philos. Mag. A **48**, 469 (1983).

[13] S. Amelinckx and P. Delavignette, Electron optical study of basal dislocations in graphite, J. Appl. Phys. **31**, 2126 (1960).

[14] N. Thompson, Dislocation nodes in face-centred cubic lattices, Proc. Phys. Soc. B **66**, 481 (1953).

[15] A. Kelly and G. Groves, *Crystallography and Crystal Defects* (Addison-Wesley, London, 1970).

[16] W. A. Sławiński, E. Zacharaki, H. Fjellvåg, and A. O. Sjåstad, Structural arrangement in close-packed cobalt polytypes, Cryst. Growth Des. **18**, 2316 (2018).

[17] Y. Barnier, R. Pauthenet, and G. Rimet, Sur la variation de l'aimantation d'un monocristal de cobalt en fonction du champ, Comptes Rendus Acad. Sci. (Paris) **252**, 3024 (1961).

[18] E. Bertaut, A. Delapalme, and R. Pauthenet, Rotation des spins dans le cobalt hexagonal, Solid State Commun. **1**, 81 (1963).

[19] E. Bertaut, A. Delapalme, and R. Pauthenet, Rotation des spins dans le cobalt hexagonal, J, Phys. (Paris) **25**, 610 (1964).

[20] J. E. Bidaux and B. Cao, Elastic behaviour of pure cobalt near the spin-reorientation phase transition, J. Phys.: Condens. Matter **3**, 2263 (1991).

[21] M. O. Steinitz, G. S. MacLeod, D. A. Pink, B. Quinn, and G. L. Ryan, Magnetoelasticity and the spin rotation transition in cobalt, Can. J. Phys. **82**, 1077 (2004).

[22] H. P. Myers and W. Sucksmith, The spontaneous magnetization of cobalt, Proc. R. Soc. London A **207**, 427 (1951).

[23] P. Fabrykiewicz, R. Przeniosło, and I. Sosnowska, Magnetic modes compatible with the symmetry of crystals, Acta Crystallogr., Sect. A: Found. Adv. **77**, 327 (2021).

[24] D. B. Litvin (ed.), *Magnetic Group Tables. 1-, 2- and 3-Dimensional Magnetic Subperiodic Groups and Magnetic Space Groups* (International Union of Crystallography, Chester, England, 2013).

[25] D. B. Litvin, Tables of crystallographic properties of magnetic space groups, Acta Crystallogr., Sect. A: Found. Crystallogr. **64**, 419 (2008).

[26] M. Hoelzel, A. Senyshyn, N. Juenke, H. Boysen, W. Schmahl, and H. Fuess, High-resolution neutron powder diffractometer SPODI at research reactor FRM II, Nucl. Instrum. Methods Phys. Res., Sect. A **667**, 32 (2012).

[27] F. Fauth, I. Peral, C. Popescu, and M. Knapp, The new material science powder diffraction beamline at ALBA synchrotron, Powder Diffr. **28**, S360 (2013).

[28] A. Bergamaschi, A. Cervellino, R. Dinapoli, F. Gozzo, B. Henrich, I. Johnson, P. Kraft, A. Mozzanica, B. Schmitt, and X. Shi, The MYTHEN detector for x-ray powder diffraction experiments at the Swiss Light Source, J. Synchrotron Radiat. **17**, 653 (2010).

[29] I. Peral, J. McKinlay, M. Knapp, and S. Ferrer, Design and construction of multicrystal analyser detectors using Rowland circles: Application to MAD26 at ALBA, J. Synchrotron Radiat. **18**, 842 (2011).

[30] F. Fauth, R. Boer, F. Gil-Ortiz, C. Popescu, O. Vallcorba, I. Peral, D. Fullà, J. Benach, and J. Juanhuix, The crystallography stations at the Alba synchrotron, Eur. Phys. J. Plus **130**, 160:1 (2015).

[31] G. Courbion and G. Ferey, $Na_2Ca_3Al_2F_{14}$: A new example of a structure with "independent F^-"–A new method of comparison between fluorides and oxides of different formula, J. Solid State Chem. **76**, 426 (1988).

[32] V. F. Sears, Neutron scattering lengths and cross sections, Neutron News **3**, 26 (1992).

[33] A. Taylor and R. W. Floyd, Precision measurements of lattice parameters of non-cubic crystals, Acta Crystallogr. **3**, 285 (1950).

[34] W. C. Ellis and E. S. Greiner, Equilibrium relations in the solid state of the iron-cobalt system, Trans. Am. Soc. Met. **29**, 415 (1941).

[35] E. A. Owen and D. M. Jones, Effect of grain size on the crystal structure of cobalt, Proc. Phys. Soc. B **67**, 456 (1954).

[36] B. E. Warren, *X-ray Diffraction*, Addison-Wesley series in metallurgy and materials engineering (Dover Publications, New York, 1990).

[37] M. Casas-Cabanas, M. Reynaud, J. Rikarte, P. Horbach, and J. Rodríguez-Carvajal, *FAULTS*: A program for refinement of structures with extended defects, J. Appl. Crystallogr. **49**, 2259 (2016).

[38] T. Roisnel and J. Rodriguez-Carvajal, A windows tool for powder diffraction patterns analysis, in Proceedings of the Seventh European Powder Diffraction Conference, EPDIC **7**, 118 (2000).

[39] G. Williamson and W. Hall, X-ray line broadening from filed aluminium and wolfram, Acta Metall. **1**, 22 (1953).

[40] V. Petříček, M. Dušek, and L. Palatinus, Crystallographic computing system JANA2006: General features, Z. Kristallogr. **229**, 345 (2014).

[41] P. Scherrer and R. Zsigmondy, *Bestimmung der inneren Struktur und der Grösse von Kolloidteilchen mittels Röntgenstrahlen*, Kolloidchemie Ein Lehrbuch (Springer Book Archives, Berlin, 1918).

[42] B. van Laar and H. Schenk, The development of powder profile refinement at the Reactor Centre Netherlands at Petten, Acta Crystallogr., Sect. A: Found. Adv. **74**, 88 (2018).

[43] H. M. Rietveld, A profile refinement method for nuclear and magnetic structures, J. Appl. Crystallogr. **2**, 65 (1969).

[44] R. Przeniosło, P. Fabrykiewicz, and I. Sosnowska, Crystal symmetry aspects of materials with magnetic spin reorientation, Acta Crystallogr., Sect. A: Found. Adv. **74**, 705 (2018).

[45] https://doi.ill.fr/10.5291/ILL-DATA.5-31-2714